Electronic Supplementary Material (ESI) for Environmental Science: Nano.

Electronic Supplemetary Information

Retention of sulfidated nZVI (S-nZVI) in porous media visualised by X-ray μ-CT - the relevance of pore space geometry

Adrian A. Schiefler[1,2,3,*], Stefan Bruns[4], Dirk Müter[3,‡], Kentaro Uesugi[5], Henning Osholm-Sørensen[3,6], Dominique J. Tobler[1,7]

[1] Nano-Science Center, Department of Chemistry, University of Copenhagen, Universitetsparken 5, 2100 Copenhagen, Denmark

[2] Groundwater Section, Capital Region of Denmark, Kongens Vænge, 3400 Hillerød, Denmark

[3] Department of Physics, Technical University of Denmark, Fysikvej, 2800 Kongens Lyngby, Denmark

[4] Institute of Metallic Biomaterials, Department for Imaging and Data Science, Helmholtz-Zentrum hereon GmbH, Max-Planck-Str. 1, 21502 Geesthacht, Germany

[5] Japan Synchrotron Radiation Research Institute, 1-1-1 Kouto, Sayo-cho, Sayo-gun, Hyogo 679-5198, Japan

[6] Xnovo Technology ApS, Galoche Alle 15, 4600 Køge, Denmark

[7] Department of Plant and Environmental Sciences, University of Copenhagen, Thorvaldsensvej 40, 1871 Frederiksberg C, Denmark

‡Present address: FORCE Technology, Park Allé 345, 2605 Brøndby, Denmark

(*Corresponding author: aalsc@dtu.dk)

Content of this supporting information

This supporting information contains additional details on methods as well as additional data and figures to support the interpretations made in the results and discussion section. In total, this SI includes 13 pages with 10 figures and 1 table.

Additional details on experiment and methods

Text S1: Additional details on the segmentation procedure and segmented phases

Region of interest (ROI) tomography often suffers from spatial heterogeneities in the reconstructed greyscale value distribution. For a consistent clean bed segmentation (pre-injection scans) these spatial variations were considered by segmenting images into material and background phase using a locally adaptive intensity thresholding routine implemented in C++. Specifically, the image stacks were traversed with 50 voxel spacing and a local threshold value was calculated with the Otsu method from all reconstructed voxels within a spherical region of 200 voxels radius. Thresholds for the skipped voxels were filled in by linear interpolation and all voxels above the computed threshold were defined to be composed of material phase, i.e., sand grains. The histograms for all voxels in the image (i.e., of the entire scan), as well as those of the segmented grains (porous matrix, PM) and pore space (PS) are shown in Fig. S1a, S1b and S1c respectively. For comparison the histograms of the segmented retained nanoparticles (NP phase) are also shown in Fig. S1d, with different y-scale for improved visibility.

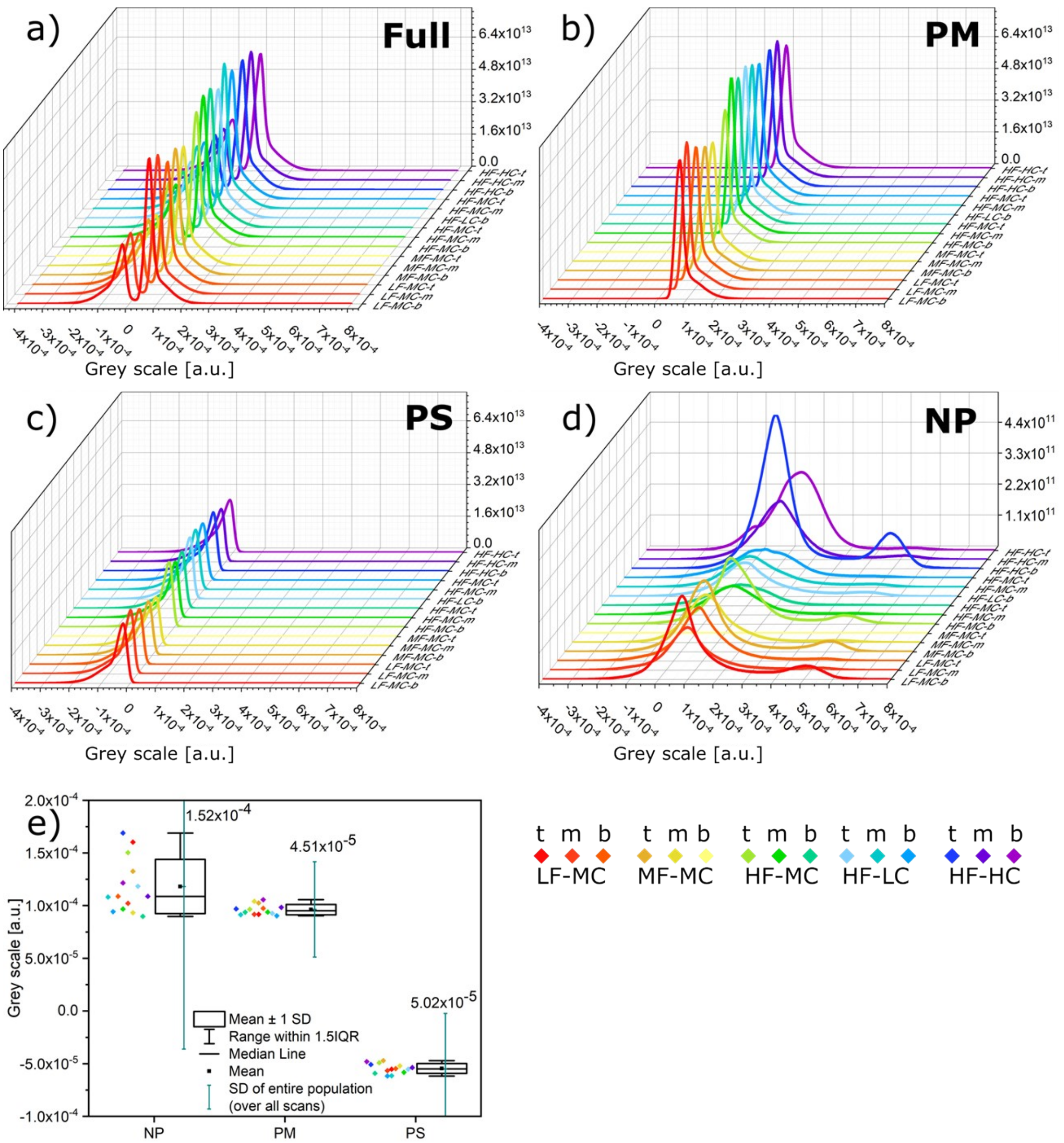

Fig. S1: Grey scale histograms a) of the full ROI of the post injection scans, and of the segmented b) porous matrix (PM), c) pore space (PS), and d) NP phase for each scanned volume of the five column experiment. Y-axis scale gives counts per bin width. e) Comparison of grey scale mean values and standard deviations (data in Table S1) between the three segmented phases and across all volumes.

Table S1: Distribution mean, mode (peak position) and standard deviation (SD) of the grey scale histograms of the segmented PM (sand grains), PS (water) and NP (S-nZVI) phase for each scanned volume, i.e., each column experiment. Mean density values (ρ) for these three phases are also given. Note the NP grey scale histograms (Fig. S2d) exhibit two peaks, and thus two modes; a primary (prim.) and secondary (sec.) mode, reflecting two NP phases varying in density (discussed in detail in the manuscript, Section 3.2.2).

		PM			PS			NP			
ρ [g/cm^3]		2.66			1.00			7.00			
histogram		mode (10^{-5})	mean (10^{-5})	SD (10^{-5})	mode (10^{-5})	mean (10^{-5})	SD (10^{-5})	prim. mode[1] (10^{-5})	sec. mode[2] (10^{-5})	mean (10^{-5})	SD (10^{-5})
LF-MC	b	7.68	9.17	3.80	-2.40	-5.53	4.79	8.27	50.91	16.02	17.25
	m	7.40	9.17	4.05	-2.40	-5.66	4.94	7.59	51.59	10.22	14.00
	t	7.96	9.74	4.14	-1.84	-5.47	5.11	8.97	52.15	10.87	13.12
MF-MC	b	8.52	10.25	4.88	-1.28	-4.71	5.16	8.28	51.70	13.25	16.33
	m	8.80	10.40	4.26	-1.28	-5.22	5.22	6.24	50.79	9.32	13.11
	t	-	-	-	-	-	-	-	-	-	-
HF-MC	b	7.96	9.64	3.89	-1.84	-4.92	4.74	9.64	48.55	15.03	14.96
	m	7.68	9.38	3.95	-2.12	-5.83	5.08	7.99	50.58	9.67	13.69
	t	7.40	9.37	4.20	-2.40	-5.92	5.08	7.47	n.d. [3]	8.97	12.64
HF-LC	b	7.40	9.26	5.74	-2.12	-5.53	4.80	6.97	46.35	11.83	16.07
	m	7.12	9.13	4.40	-2.68	-6.14	5.05	6.10	48.60	10.81	15.37
	t	7.12	9.03	6.28	-2.96	-6.17	5.10	8.38	37.81	9.42	14.23
HF-HC	b	8.24	9.68	4.08	-1.84	-5.09	4.79	9.81	49.02	16.88	16.87
	m	8.24	9.83	4.08	-1.56	-5.38	5.10	8.52	51.54	10.88	13.84
	t	8.80	10.56	4.33	-1.00	-4.81	5.12	13.41	50.06	12.15	11.60
Mean		7.93	9.62	4.43	-1.94	-5.45	5.01	8.05	49.32	11.81	14.51
SD		0.55	0.48	-	0.55	0.45	-	1.75	3.65	2.48	-

[1]mode of the primary, low density NP phase; [2]mode of the secondary, high density NP phase; [3] n.d. means: not determined, i.e. no secondary maximum exists.

Text S2: Local registration/warping of the reconstructions after injection.

A global rigid body registration does not match the post-injection volume with the pre-injection volume because pressure variations upon injection of the S-nZVI particles caused a local rearrangement of the granular packing. Movement was primarily observed along the column axis as shown for each scan in Fig. S2. Positions in the upper part of the column experienced generally more translation than the bottom position. Variations in rigidity, tightness of packing, permeability and pressure build-up, due to S-nZVI retention, may have all affected the extent of movement. Particularly rearrangements (spatial relaxation) at the fine/coarse sand interface likely initiated movement in the first place.

We achieve the local motion estimation by masking out the pre-injection pore space and calculating the voxel level optical flow between the scans before and after injection. The resulting field of displacement vectors is then used to warp the post-injection scan towards the pre-injection state.

We calculated optical flow with a custom CUDA-C++ multiscale variational solver that provides a 4D extension to the concepts introduced by Brox et al. [1]. The core of our algorithm is designed after the 4D optical flow implementation of Ershov [2] [3], using an inner/outer iteration scheme [1] and accelerated by successive over-relaxation as described by Liu for sequences of 2D images [4]. Briefly, the energy functional to be minimized is of the form:

$$E(u) = E_{Data} + \alpha \cdot E_{Smoothness} \tag{1}$$

where the data term E_{Data} is constrained to provide a non-linear intensity constancy assumption [1] and the smoothness term $E_{Smoothness}$ enforces a piecewise constancy constraint. Anisotropic flow-driven regularization was chosen for $E_{Smoothness}$ [5] and a regularizer function $\Psi(s^2)$ was applied to both the data and the smoothness term as a concave function of the form $\Psi(s^2) = \sqrt{s^2 + \epsilon^2}$ with ϵ being a small constant, leading to a robust penalizer.

All input data were normalized and a deliberately high regularization parameter α of 0.2 was chosen for eqn. 1, such that the motion of the grains was smoothly interpolated in the pore space. Larger grain displacements (such as observed in HF-HC column, Fig. S3) were tracked by traversing an image pyramid of up to 18 levels with a scaling factor of 0.8 between scales. Gradients were approximated as fourth order central finite difference and warping between outer iterations and pyramid scales was performed with tricubic interpolation.

At the lower pyramid levels GPU memory limitations required us to divide the data into patches with 100 voxels of overlap that were synchronized between outer iterations. This severely slowed down the solution process. A 1024x1024x1024 voxel displacement field could however be calculated in ~1 h on a single 32 GB Tesla V100 graphic card and proofed to be sufficiently accurate to be upsampled and applied to the 2048x2048x2048 input data. The warped data nevertheless exhibited a slight mismatch at the PM-PS interface, as a result of which the outer 1 µm around the clean bed grains (PM) were discarded in the subsequent NP segmentation.

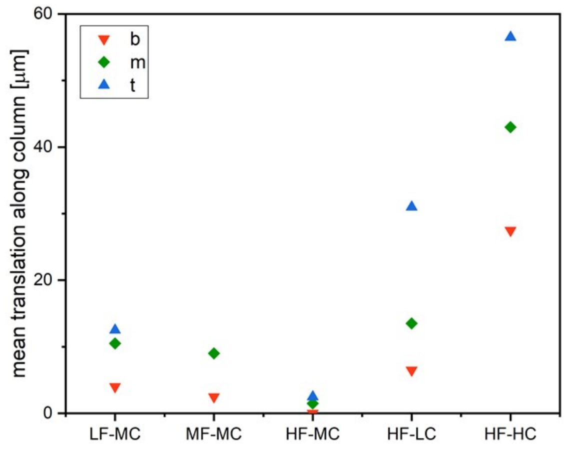

Fig. S2: Mean translation of the volume along the column length (upward movement) for all analysed volumes, i.e., column experiments.

Text S3: Size analysis of retained S-nZVI structures

The size of the retained S-nZVI structures was estimated by adding up all NP voxels connected via faces, edges or corners. Fig. S3a shows the structure size (in μm^3) for 50 % and 95 % of the total retained NP volume (i.e., 50^{th} and 95-percentile respectively), while in Fig. S3b, only NP voxels of the secondary, high density NP phase (described in Section 3.2.2 in the manuscript) were included for structure size analysis. In Fig. S3c, the volume of retained NP (V%(PS)) was plotted against the 50^{th} and 95^{th} percentile structure sizes and then fitted using linear correlation (black and red fits respectively). For NP retention via a ripening process, the retained NP volume would be expected to increase exponentially with structure size (power model) [6]. For depth dependent straining an exponential decline with column depth would be expected if the structures measured were retained as single colloids. The former is indeed found (data not shown but similar trends as for RCPs, Fig. 6 main text), albeit the latter is being disputed by us.

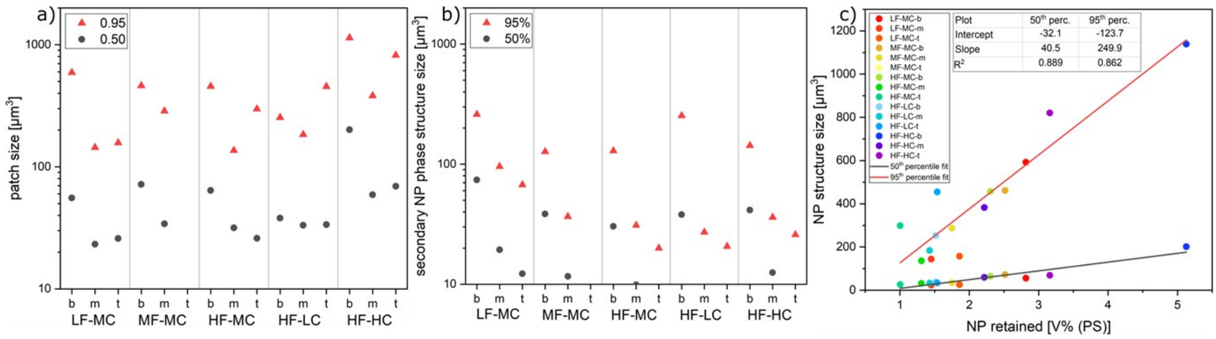

Fig. S3: Analysed sizes of retained S-nZVI structures for all column volumes if including a) all NP voxels or b) only NP voxels assigned to the secondary, high density NP phase. Shown are the sizes by which 50 % (median size) and 95 % of the total retained NP volume of a scan is accounted for (50- and 95-percentile, respectively). c) Linear correlations between the total volume of retained NP (i.e. V%(PS)) and the 50- and 95-percentile NP structure sizes. The red fit shows the 95th percentile, the black fit the 50th percentile.

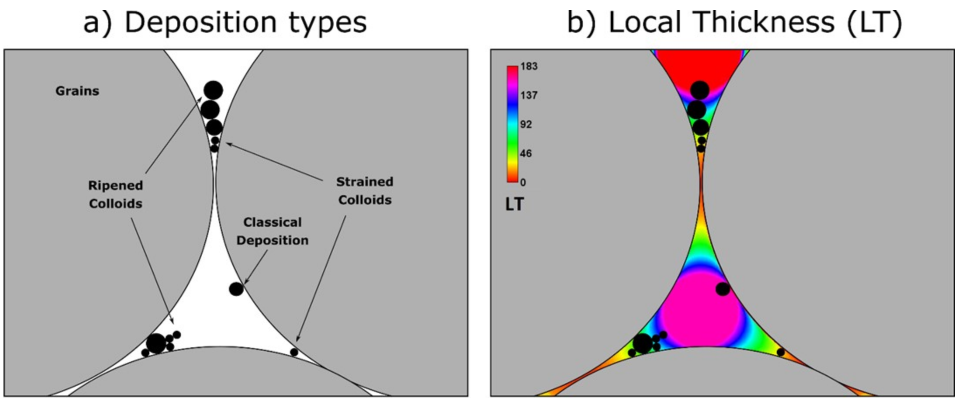

Fig. S4: Visualisation of a) different spatial retentions for different retention mechanisms within a pore and b) the relation to the local thickness (LT) values occupied by the respective colloids. A single strained colloid would occupy LT values in the range of its diameter, whereas a classical (pure DLVO) retention within the pore body results in high LT values. Ripened colloids, attaching to strained ones, will gradually occupy increasingly higher LT values.

Text S4: Additional details on flow modelling

Hydrodynamic flow fields were calculated in the pre-injection reconstructions with the Lattice Boltzmann method (LBM) for a single component of density ρ=1.0 on cylindrical volumes of 1800 voxels diameter that were down-sampled by a factor of 2 once because of computer memory limitations. We used a D3Q19 velocity set with two-relaxation-time collision, a magic number of 1/4 and a relaxation parameter τ=1.0, which collectively translates to a dynamic viscosity of 1/6. Zero flow interfaces were modelled by placing halfway bounce back nodes on the grain voxels that interface with the pore space. Dirichlet pressure boundaries were placed at the top and bottom exterior boundaries of the image stack to drive the fluid upwards. The first and the last slice were replicated 5 times for minimizing inlet/outlet effects. All other exterior boundaries were treated to be zero flow boundaries.

The pressure boundaries were adjusted to replicate the experimentally observed modified Reynolds number *Re* within a 1% error interval defined as:

$$Re = \frac{\rho \, u_{sup} \, L}{\mu \, (1 - \phi)} \tag{2}$$

where ϕ denotes porosity, u_{sup} the superficial velocity and L the average particle diameter of 112.5 µm. The density of the injected slurry ρ was estimated as 1.07 g/cm^3 and the dynamic viscosity μ as 50 cP which results in *Re* on the scale of $2 \cdot 10^{-3}$(i.e., creeping flow regime), meaning flow is dominated by viscous effects.

Similar to the optical flow computations, all LBM simulations were performed with a custom CUDA-C++ implementation and executed on a single Nvidia Tesla V100 graphic (32 Gb) card yielding a stable solution in a matter of minutes.

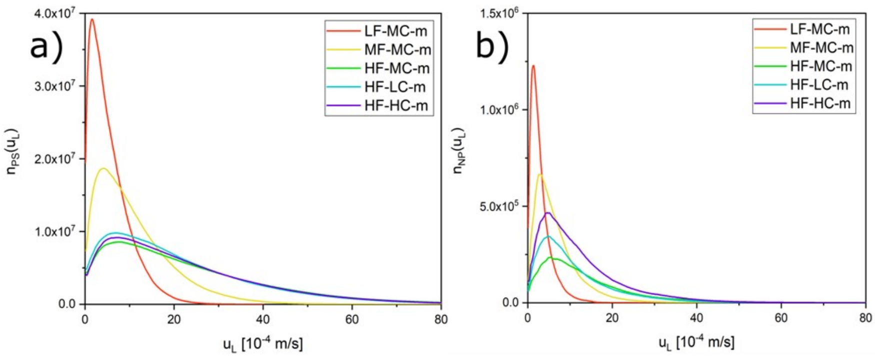

Fig. S5: Distributions of local flow velocities a) in the clean bed pore space ($n_{PS}(u_L)$), and b) for the voxel set classified as NP ($n_{NP}(u_L)$), for all middle column positions.

Text S5: TEM experimental details

The TEM sample was prepared by drop-casting 3 µl of a freshly prepared and highly concentrated nZVI suspension (in ethanol) on formvar coated copper TEM grids. The sample was analyzed on a Philipps

CM20, at an accelerating voltage of 200 kV. nZVI was prepared in the same way as S-nZVI, but without the sulfidation treatment.

Additional details on pore space characterization and spatial NP retention

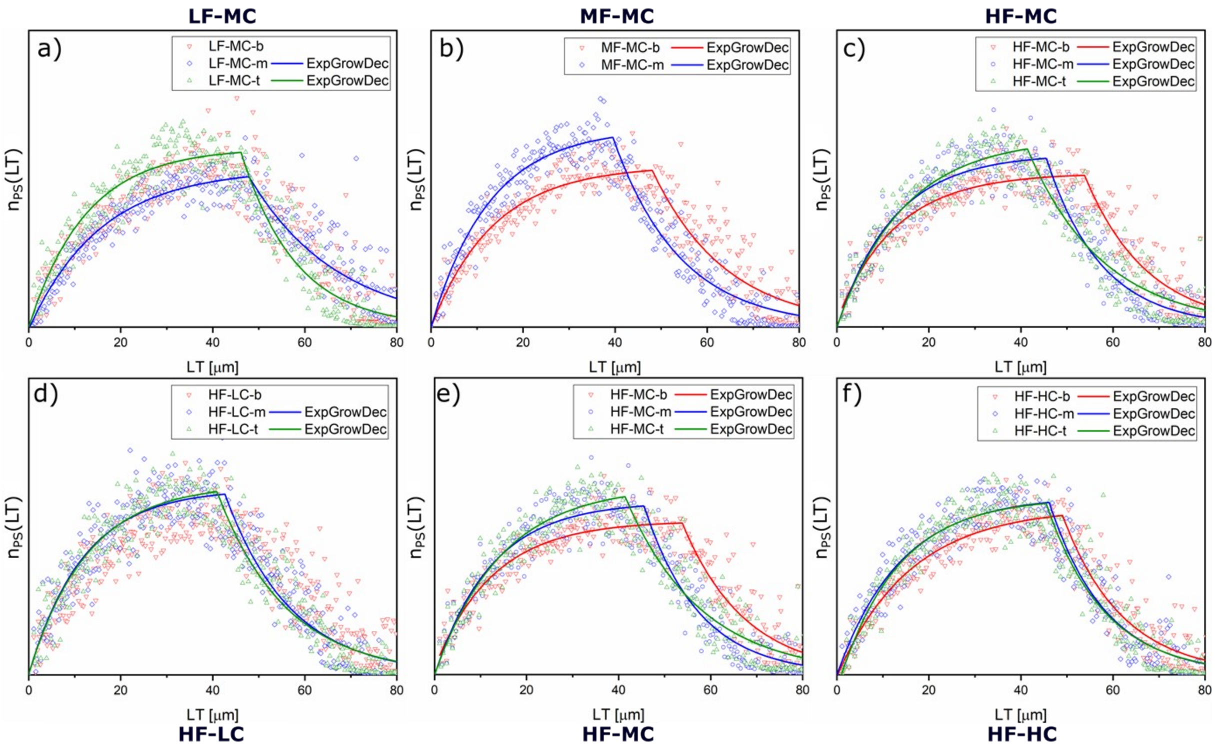

Fig. S6: Distributions of pore space local thickness (n_{PS}(LT)) for all volumes, i.e., column experiments: a) LF-MC, b) MF-MC, c) HF-MC, d) HF-LC, e) HF-MC (same as c), f) HF-HC. Exponential growth and decay models have been fitted to the distributions, where possible, to ease comparison. Note that differences between distributions are due to variations in the pore geometry between volumes, and not because of the different applied injection conditions.

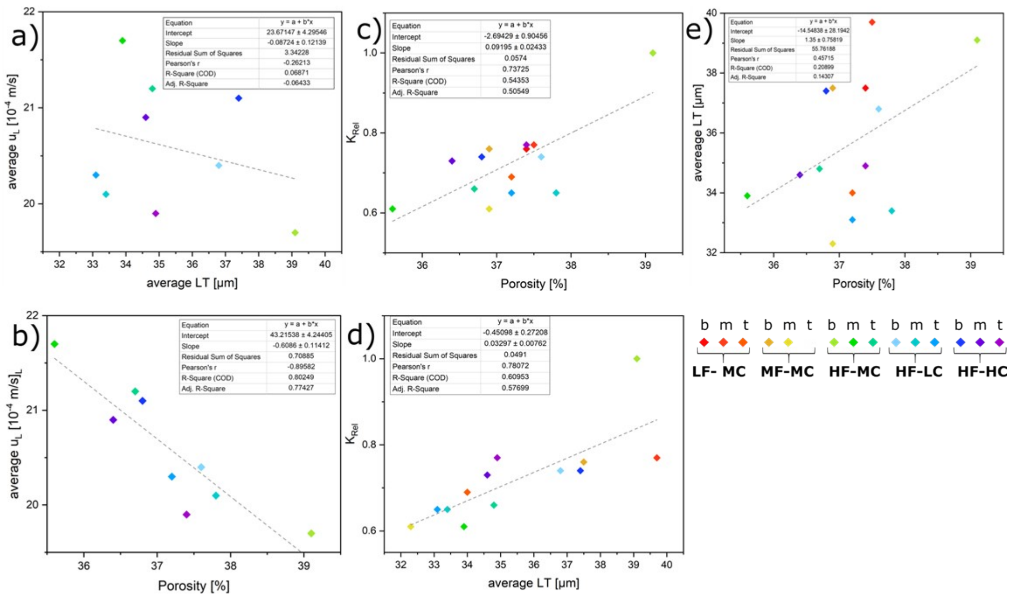

Fig. S7: Correlations between different pore geometry and flow properties obtained for the analysed volumes. Average local flow velocity, u_L, as a function of (a) average LT and (b) porosity; relative permeability (K_{Rel}) as a function of (c) porosity and (d) average LT; and (e) correlation between average LT and porosity values.

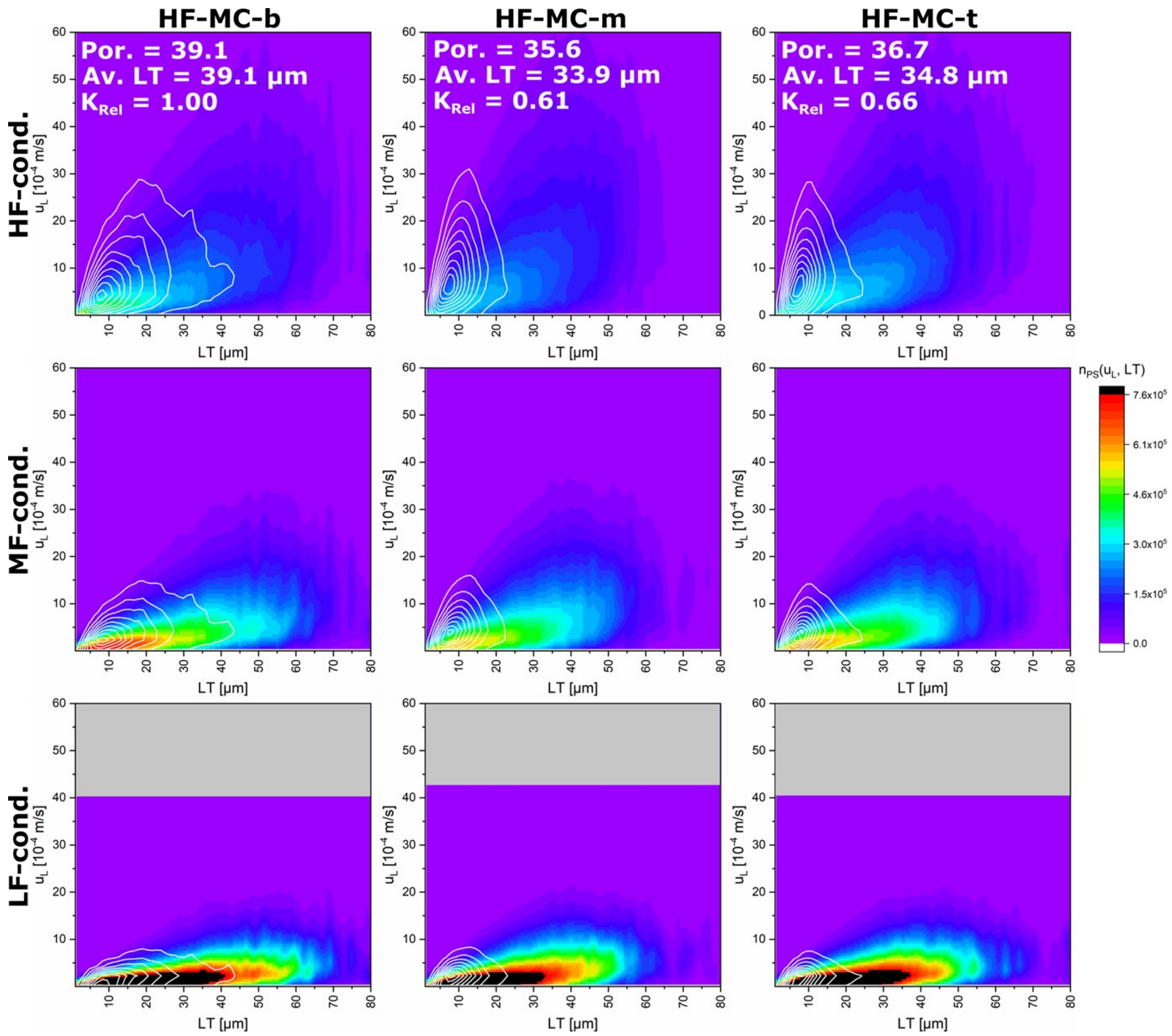

Fig. S8: 2D histograms of n_{PS} (LT, u_L) for the bottom, middle and top volume (left to right) of the HF-MC column. The flow velocity distribution was modelled using different superficial flow velocities; matching HF ($5.8x10^{-4}$; top row images), MF ($2.9x10^{-4}$; middle row images), and LF ($1.5x10^{-4}$; bottom row images) conditions. The 2D histograms are overlayed by white iso contour maps (increments between contours are a tenth of the respective maximum value) that show the NP retention probability $P_{Ret}(u_L, LT)$ for the HF-MC experiment, as an example, in the three volumes under varying modelled flow regimes. For each geometry, values for porosity (por.), average LT and relative permeability ($K_{Rel.}$) are given in the plots of that geometry.

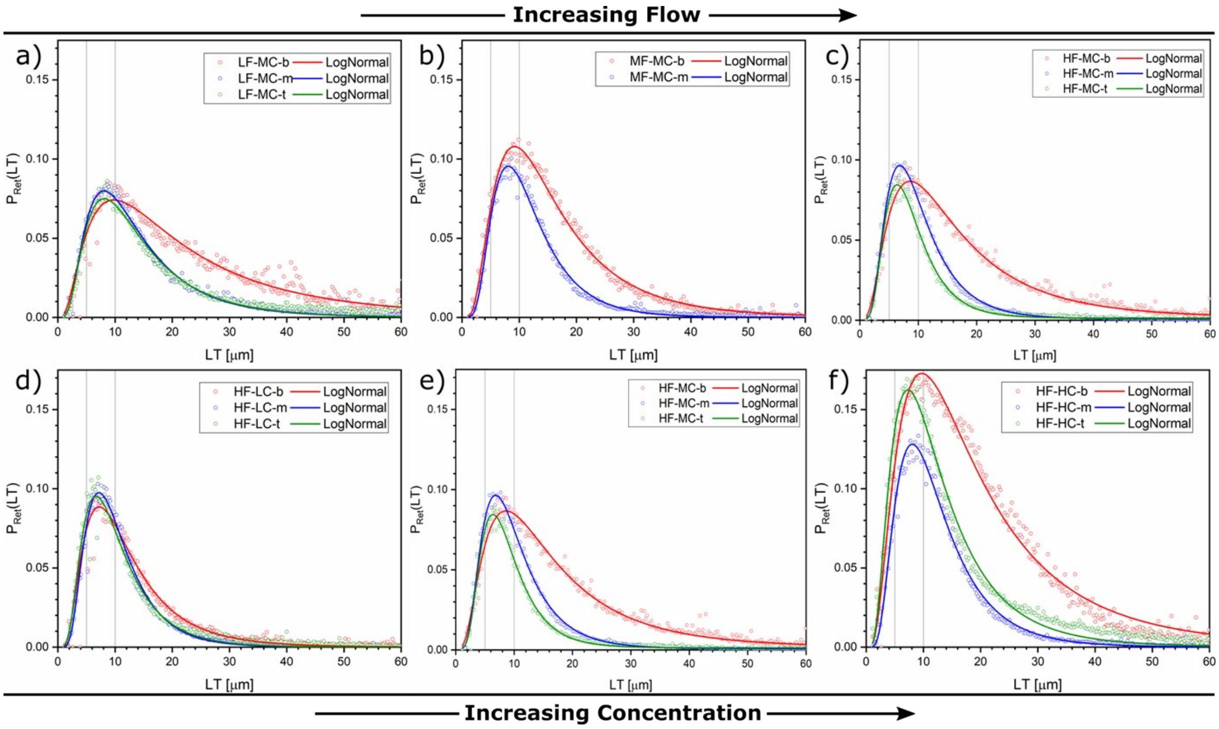

Fig. S9: $P_{Ret}(LT)$ distributions of columns run at different flow rates and medium S-nZVI concentration (top row): a) LF-MC, b) MF-MC and c) HF-MC. Columns run at different S-nZVI concentrations and high flow rate, HF (bottom row): d) HF-LC, e) HF-MC, f) HF-HC.

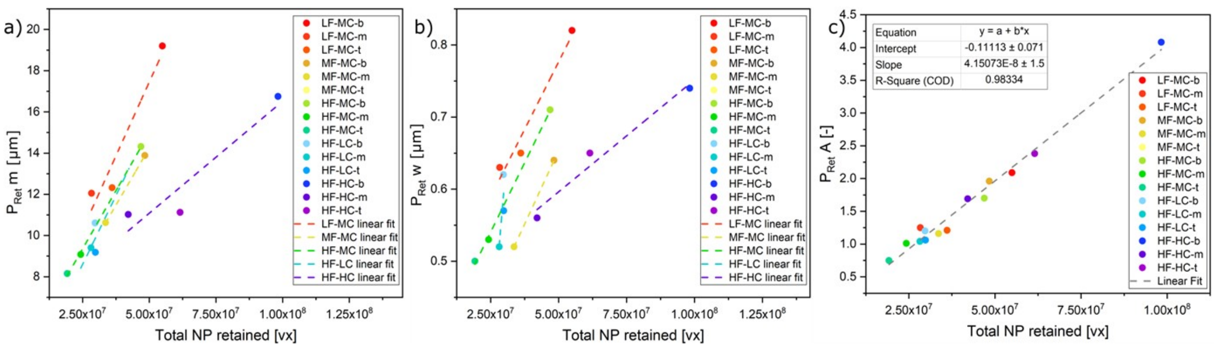

Fig. S10: Correlations between the total number of NP voxels and the parameters derived from log-normal fitting of $P_{Ret}(LT)$: a) mean LT value (m), b) standard deviation (w), and c) area factor (A). In a) and b) linear fits were added (dashed lines) to each set of volumes of a column experiment, while in c) all data were included in one linear fitting.

References

[1] T. Brox, A. Bruhn, N. Papenberg and J. Weickert, “High Accuracy Optical Flow Estimation Based on a Theory for Warping,” in *Computer Vision – ECCV 2004*, 2004, pp. 25-36.

[2] A. Ershov, “Automated Analysis of Time-Resolved X-ray Data usin Optical Flow Methods,” Karlsruher Institut für Technologie, Karlsruhe, 2015.

[3] T. dos Santos Rolo, A. Ershov, T. van de Kamp and T. Baumbach, “In vivo X-ray cine-tomography for tracking morphological dynamics,” *PNAS,* vol. 111, no. 11, pp. 3921-3926, 2014.

[4] C. Liu, “Beyond Pixels: Exploring New Representations and Applications for Motion Analysis,” Massachusetts Institute of Technology, 2009.

[5] J. Weickert and C. Schnörr, “A Theoretical Framework for Convex Regularizers in PDE-Based Computation of Image Motion,” *International Journal of Computer Vision,* vol. 45, no. 3, pp. 245-264, 2001.

[6] R. S. T. Tosco, “Transport of non-newtonian suspensions of highly concentrated micro- and nanoscale iron particles in porous media: A modeling approach,” *Environ. Sci. Technol.,* vol. 44, p. 9062–9068, 2010.

[7] B. Ohnesorge, T. Flohr, K. Schwarz, J. P. Heiken and K. T. Bae, “Efficient correction for CT image artifacts caused by objects extending outside the scan field of view,” *Medical Physics,* vol. 27, no. 1, pp. 39-46, 1 2000.

[8] B. Münch, P. Trtik, F. Marone and M. Stampanoni, “Stripe and ring artifact removal with combined wavelet-Fourier filtering,” *EMPA Activities,* vol. 17, no. 2009-2010 EMPA ACTIVITIES, pp. 34-35, 11 5 2009.

[9] D. Gürsoy, F. De Carlo, X. Xiao and C. Jacobsen, “TomoPy: A framework for the analysis of synchrotron tomographic data,” *Journal of Synchrotron Radiation,* vol. 21, no. 5, pp. 1188-1193, 2014.

[10] S. A. Bradford, J. Simunek, M. Bettahar, M. T. Van Genuchten and S. R. Yates, “Significance of straining in colloid deposition: Evidence and implications,” *Water Resources Research,* vol. 42, no. 12, 1 12 2006.

[11] R. Chityala, K. R. Hoffmann, S. Rudin and D. R. Bednarek, “Artifact reduction in truncated CT using Sinogram completion,” *Proc SPIE Int Soc Opt Eng.,* vol. 5747, no. 3, pp. 2110-2117, 2005.

[12] S. Bruns, S. L. S. Stipp and H. O. Sørensen, “Looking for the Signal: A guide to iterative noise and artefact removal in X-ray tomographic reconstructions of porous geomaterials,” *Advances in Water Resources,* vol. 105, pp. 96-107, 2017.

[13] E. X. Miqueles, J. Rinkel, F. O'Dowd and J. S. V. Bermúdez, “Generalized titarenko’s algorithm for ring artefacts reduction,” *Journal of Synchrotron Radiation,* vol. 21, no. 6, pp. 1333-1346, 2014.